Received: 18 October 2023 | Revised: 25 June 2024 | Accepted: 8 July 2024

DOI: 10.1002/jsp2.1361

RESEARCH ARTICLE

JOR Spine OPEN ACCESS

Three-dimensional fiber patterning in the annulus fibrosus can be derived from vertebral endplate topography

Ali Raza | Gwynneth T. Howell | Arthur J. Michalek

Department of Mechanical & Aerospace Engineering, Clarkson University, Potsdam, New York, USA

Correspondence
Arthur J. Michalek, Department of Mechanical & Aerospace Engineering, Clarkson University, Box 5725, Potsdam, NY 13699, USA.
Email: ajmichal@clarkson.edu

Funding information
Directorate for Engineering, Grant/Award Number: 2138342

Abstract

Introduction: The annulus fibrosus (AF) of the Intervertebral disc (IVD) is composed of concentric lamellae of helically wound collagen fibers. Understanding the spatial variation of collagen fiber orientations in these lamellae, and the resulting material anisotropy, is crucial to predicting the mechanical behavior of the complete IVD.

Methods: This study builds on a prior model predicated on path-independent displacement of fiber endpoints during vertebral body growth to predict a complete, three-dimensional annulus fibrosus fiber network from a small number of subject-independent input parameters and vertebral endplate topographies obtained from clinical imaging. To evaluate the model, it was first fit to mid-plane fiber orientations obtained using polarized light microscopy in a population of bovine caudal discs for which computed tomography images vertebral endplates were also available. Additionally, the model was used to predict the trajectories based on human lumbar disc geometries and results were compared to previously reported data. Finally, the model was employed to investigate potential disc-related variations in fiber angle distributions.

Results: The model was able to accurately predict experimentally measured fiber distributions in both bovine and human discs using only endplate topography and three input parameters. Critically, the model recapitulated previously observed asymmetry between the inclinations of right- and left-handed fibers in the posterolateral aspect of the human AF. Level to level variation of disc height and aspect ratio in the human lumbar spine was predicted to affect absolute values of fiber inclination, but not this asymmetry.

Conclusion: Taken together these results suggest that patient-specific distributions of AF fiber orientation may be readily incorporated into computational models of the spine using only disc geometry and a small number of subject-independent parameters.

KEYWORDS
biomaterials, development, growth

1 | INTRODUCTION

The outer annulus fibrosus (AF) of the intervertebral disc (IVD) consists of concentric lamellae composed primarily of type I collagen fibers arranged in alternating right- and left-handed helices. The AF maintains a robust connection between adjacent vertebral bodies while constraining hydraulic swelling of the nucleus pulposus (NP) and allowing flexibility of the spinal column. The layered structure of the AF results in a high degree of mechanical anisotropy,[1] which is sensitive to the relative orientations of the fibers in adjacent lamellae. Understanding the spatial distribution of fiber orientations in the AF is thus essential for predicting the mechanical behavior of the whole disc.[2–6]

While the fibers of the AF are often described as being oriented at an inclination of 30° from horizontal, there have been numerous observations of spatial variation.[7–11] In particular, it has been seen in all species studied that fiber inclination is steeper relative to the transverse plane in the inner AF than the outer. It has further been suggested by our group that this radial trend is opposite of what would be predicted in an AF optimized to contain NP swelling pressure.[10] Of additional interest is the observation by Marchand and Ahmed that in some parts of the human lumbar disc, specifically posterolateral, right- and left-handed fibers do not have the same inclination angle.[12] Coincidentally, this location experiences both the highest fiber strains[13] and highest incidence of herniation[14] in the disc. Typical measurements of AF fiber inclination are destructive, depending on either visual inspection,[12,15] histology,[9,10] or high energy x-ray imaging.[16] Diffusion tensor magnetic resonance imaging has shown some promise for in-vivo fiber orientation measurement, but has so far required higher magnetic fields than clinically practical.[11,17] Taken together, these findings suggest a sub-optimal material structure and raise questions both about how it evolved and how it may be predicted and incorporated into a subject-specific finite element model.

A growth-based model has recently been proposed to describe the spatial distribution of fiber orientations in the AF.[9] Briefly, this model assumes populations of right- and left-handed helical fibers in the thin notochordal sheath, the end-points of which become anchored into the developing vertebral bodies. As the spine grows, these points move outwards radially and apart axially. Insertions of AF fibers into the vertebral endplates[18–21] suggest that fibers are unable to re-orient through circumferential endpoint movement. As fiber endpoint position is constrained, the model proposes a process that is path independent. Thus, the distribution of fibers in any state is dependent only on the geometry of that state. While this model has been successfully used to describe mid-height fiber angle distributions in mouse caudal, bovine caudal, and human lumbar discs, it has not yet been applied to the full three-dimensional distribution. As both axial variability in fiber orientation and areas of right- and left-handed asymmetry have been observed in the human lumbar AF,[12] a full three-dimensional distribution of fiber orientations is essential for understanding the role of material anisotropy in the mechanical function of the IVD.

The goal of this study was to test such a model's ability to generate a full, three-dimensional annulus fibrosus fiber network using only vertebral endplate topographies obtainable through clinical imaging and a small number of subject independent input parameters. This study builds upon the growth-based fiber orientation theory by generating AF fiber trajectories along virtual lamellar surfaces, connecting pairs of points on the superior and inferior vertebral endplates. The model was first validated by generating fiber trajectories from computed tomography scans of bovine tails and comparing predicted fiber orientations to those measured via polarized light microscopy. The objective of this portion of the study was to test the model's ability to fit a data set from which vertebral endplate topographies and mid-plane fiber angles are known for the same discs. The model was further used to generate trajectories based on human lumbar disc geometries, with comparison to previously published observations. Finally, the model was used to probe potential variation in fiber angle distributions depending on disc geometry. The objectives of this portion of the study were to test the ability of the model to recapitulate observed three-dimensional trends in fiber orientation in the human AF and to test the degree to which they may be expected to vary with geometric differences between individual discs. In addition to elucidating the mechanisms through which the complex structure of the AF forms, such a model will allow patient specific computational modeling of the IVD with accurate anisotropic material behavior.

2 | METHODS

2.1 | Model development

A three-dimensional model was constructed in MATLAB (code provided in the supplemental material, Data S1) to produce a predicted three-dimensional fiber angle distribution based on a pair of vertebral endplate topographies and a minimal number of input parameters. The model assumes that the disc in the early growth state is a uniform, thin-walled cylinder, with the circumferential positions of fibers in the cylinder fixed where they intersect the vertebral endplates. The circumferential distance between a fiber's superior and inferior endpoints is defined here as the fiber span angle. While fiber span angle (Figure 1A) is assumed to remain the same in any given virtual lamella it can change linearly from inner to outer AF. Thus, the fiber span angle (θ_S) is defined as a function of nondimensional radial position (ranging from zero at inner to one at outer) by span angle at the inner virtual lamella (θ_{SI}), and fiber span angle slope ($\Delta\theta_S$). A positive value of span angle slope indicates that fiber span angle increases from inner to outer AF. During growth, anchored fiber end points were assumed to move radially outward and axially apart as the spine grew. The model assumes that fiber endpoint displacement is path independent. As a result, fiber angle predictions will depend only on the geometry of the disc in its current state, not any of the preceding growth states. As the shape of the mature human lumbar disc is asymmetric anterior to posterior, fiber angle predictions will depend on the placement of the center axis from the early state to the mature state.[9] In the present model this is accounted for by an origin shift in the mid-sagittal plane, relative to halfway between the anterior-most and posterior-most points in the outer annulus. Positive value of origin

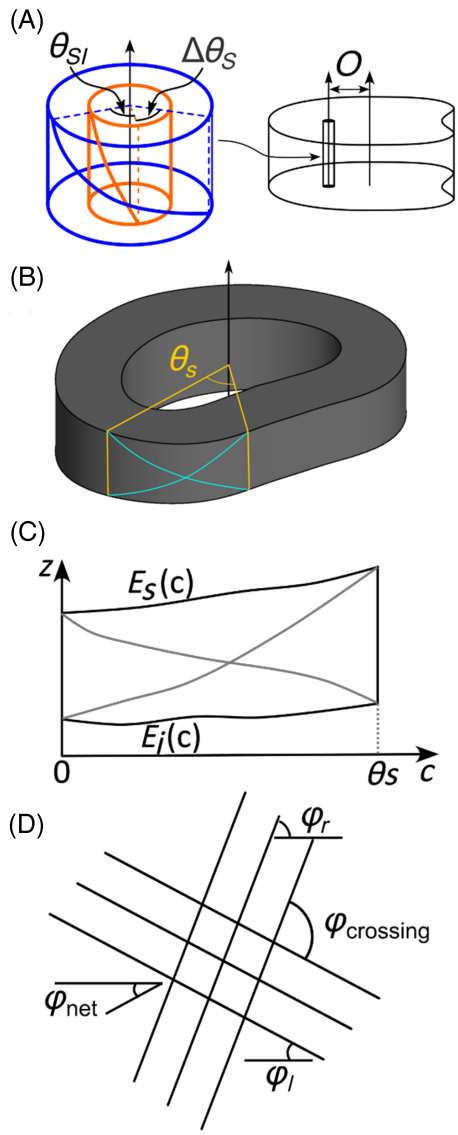

FIGURE 1 The model assumes that fibers originate in a thin-walled cylinder with inner fiber span angle of θ_{SI}, change of span angle from inner to outer of $\Delta\theta_S$, and offset from mature center, O (A). Upon growth, the fibers are projected in the curved plane of a virtual lamella, from endplate to endplate across an angular span of θ_S (B). By unwrapping this lamellar segment into axial-circumferential coordinates, the axial positions along the lengths of right- and left-handed fibers are projected relative to inferior and superior elevations (E_i and E_s, respectively (C). At any point (D). The right- and left-handed inclination angles (φ_r and φ_l, respectively) can be used to calculate fiber crossing angle ($\varphi_{crossing}$) and net fiber angle (φ_{net}).

shift indicates that the origin is shifted toward posterior and negative indicates that origin is shifted toward anterior. These three parameters, which are presumed to be subject independent, may be varied to produce a best fit of fiber angle predictions to experimental values. For a given set of parameters, the outer and inner AF cartesian coordinates of a disc are converted to cylindrical coordinates relative to the origin and fit using an 8th order Fourier series. A user-defined number of virtual lamellae are then evenly distributed between inner and outer AF, each also defined by an 8th order Fourier series. Both inferior and superior endplates surfaces are smoothed using a Lowess fit with a span of 10%. These virtual lamellae are used to homogeneously predict right- and left-handed fiber distributions at defined points in three-dimensional space. The current model makes no assumptions about actual thickness or continuity of lamellae in the disc and assumes that radial bulging between the endplates is small.

Around each virtual lamella, a series of 100 overlapping segments with span angle, θ_S, are defined as shown in Figure 1B. For each segment, Delaunay triangulation of superior and inferior endplates is used to interpolate intersections between the Fourier series describing the virtual lamella and the endplates at 50 points each. This segment is then unwrapped into axial–circumferential (z–c) coordinates. A pair of fibers is then projected between opposite corners of the segment as shown in Figure 1C. First, the interpolated lines of intersection between the virtual lamellar profile and the inferior and superior endplates are defined as elevations E_i and E_s, respectively. The elevations of the right- and left- handed fibers (E_R and E_L, respectively) are then defined by Equations (1) and (2), where c is local circumferential coordinate.

$$E_R(c) = E_i(0) + \frac{c}{\Theta_S}(E_s(\Theta_S) - E_i(0)), \tag{1}$$

$$E_L(c) = E_s(0) - \frac{c}{\Theta_S}(E_s(0) - E_i(\Theta_S)). \tag{2}$$

The fiber inclination angles for both right- and left-handed fibers (φ_r and φ_l, respectively) are calculated using Equations (3) and (4), respectively.

$$\varphi_r = \tan^{-1}\left(\frac{E_R(c)}{c}\right), \tag{3}$$

$$\varphi_l = \tan^{-1}\left(\frac{E_L(c)}{c}\right). \tag{4}$$

Inclination angles for fibers projected across each segment of the virtual lamella are then transformed to global circumferential coordinates and compiled. The values are interpolated onto an 20 × 100 grid covering the full virtual lamella and used to calculate net fiber angle (φ_{net}) and fiber crossing angle ($\varphi_{crossing}$) using Equations (5) and (6) (Figure 1D).

$$\varphi_{net} = \varphi_r - \varphi_l, \tag{5}$$

$$\varphi_{crossing} = \varphi_r + \varphi_l. \tag{6}$$

2.2 | Prediction of bovine fiber angles

The fiber projection model was first fit to experimental measurements of mid-plane fiber crossing angles reported previously by Michalek.[9]

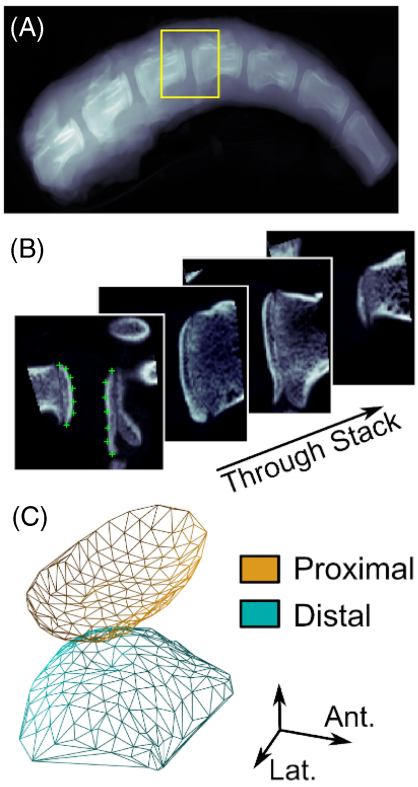

FIGURE 2 From CT scans of bovine tails (A) stacks were extracted around each disc (B) and digitized to generate three-dimensional endplate contours (C).

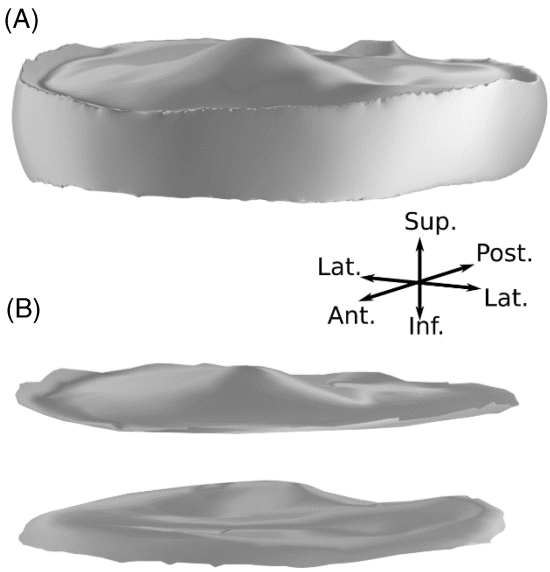

FIGURE 3 Representative human lumbar L4L5 disc (A) with superior and inferior endplate surfaces isolated (B).

Additionally, clinical CT scans of the five tails from which the discs in that study were harvested had been obtained by Duclos et al. for the measurement of muscle cross-sections.[22] In the present study, those scans (LightSpeed VCT, GE Healthcare, Waukesha, WI, with 0.3 mm in-slice pixel size and 0.45 mm spacing between slices) were re-analyzed as follows to obtain vertebral endplate surfaces.

Computed tomography scans were imported into MATLAB and manually processed as follows. First, a lateral projection of the three-dimensional image was used to identify a region of interest around a particular disc (Figure 2A). A stack of sagittally oriented images in the region of interest was then used to manually select points on the proximal and distal endplates (Figure 2B). This process was then repeated using a stack of coronally oriented images. These points were used to generate proximal and distal endplate surfaces (Figure 2C), which had an average of 309 coordinate points.

Sixteen discs (levels c1c2 through c5c6) from five tails were digitized for endplate topographies. The outer AF profile was assumed to be a cylinder with a diameter based on caliper measurement at the time of dissection. The inner AF was defined as an ellipse in the model, with dimensions taken from photographs of the transected discs. Predicted fiber angles were calculated by dividing the model virtual lamellae equally into three zones (inner, middle, outer) consisting of 10 virtual lamellae each. Posterior, anterior, and lateral regions were defined by dividing the virtual lamellae into 90° segments. Mean values of left-handed and right-handed fiber angles were calculated across each of the nine region-zone combinations to yield a total of 144 predicted average crossing angles.

Experimental fiber angles were measured by digitizing cross-polarized micrographs of thin sections of AF taken from the inner, middle, and outer zones of the posterior, anterior, and lateral disc regions as previously reported[9] similarly yielding a set of 144 experimental crossing angles. As exact radial position or lamellar number of the imaged slices was not recorded, they were assumed to be average for their region and zone. Optimal values of origin shift, fiber span angle at inner virtual lamella (θ_{SI}), and span angle slope ($\Delta\theta_S$) from inner to outer AF were found by minimizing error between all 144 pairs of predicted and measured fiber crossing angles simultaneously using a simplex algorithm. Goodness of fit was assessed by linear regression of predicted to measured fiber crossing angles.

2.3 | Prediction of human fiber angles

Human lumbar disc geometries were acquired from an online database (BodyParts3D, © the Database Center for Life Science licensed under CC Attribution-Share Alike 2.1 Japan). The human L4L5 disc is shown in Figure 3A. The superior and inferior endplates (each consisting of 1444 coordinate points) were manually separated from the rest of the disc geometry as shown in Figure 3B.

The disc's outer AF profile was defined by identifying points in the transverse plane lying within the outer edges of both endplates. The innermost virtual lamella was defined by scaling down the outer profile such that the NP covered 30% of the area of the disc. The AF was then defined by 30 evenly distributed virtual lamellae. Net angles and crossing angles were calculated by evaluating Equations (1)–(6) on these virtual lamellae. Optimal values of origin shift, fiber span angle at inner virtual lamella, and span angle slope from inner to outer AF were

TABLE 1 Morphometry of the four modeled human lumbar discs.

Disc	Average height (mm)	Anterior–posterior (mm)	Lateral (mm)	Aspect ratio (A-P/L)
L1L2	6.57	36.91	40	0.92
L2L3	7.08	35.53	42.77	0.83
L3L4	6.14	37.96	44.46	0.85
L4L5	8.35	37.55	47.45	0.79

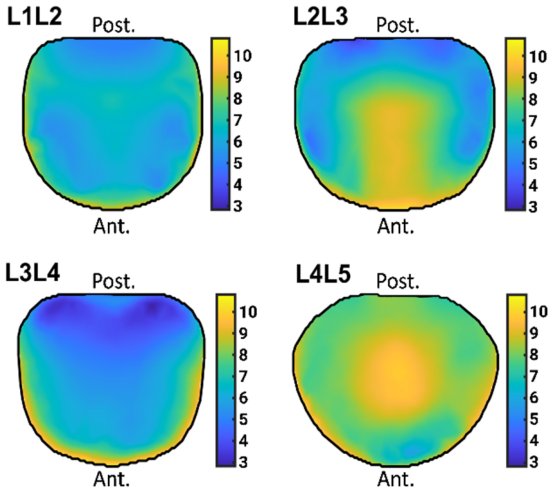

FIGURE 4 Height maps of four representative human lumbar discs. Color bars indicate height in millimeters.

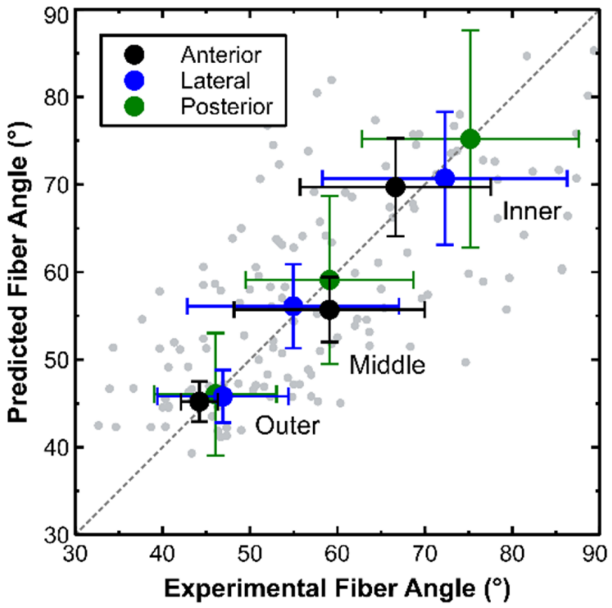

FIGURE 5 Comparison of mean experimental and model fiber crossing angle values (±SD). Gray circles indicate all individual data points. Dashed line indicates 1:1.

calculated by varying their values using a simplex algorithm in order to minimize the error between model predicted right- and left-handed crossing angle and observed fiber angles reported by Holzapfel et al.[15] at the same 18 locations. While the endplate topographies of the disc in that study are not available, it had an AP-Lateral aspect ratio of 0.72, which is comparable to the modeled disc's aspect ratio of 0.79.

2.4 | Prediction of level effect

To study the effect of disc geometry, optimal model parameter values found above were applied to three other lumbar disc geometries from the database (L1L2, L2L3, L3L4). As the model described in Section 2.1 depends on both radial and axial positions of fiber endpoints, these discs were chosen to represent a range of transvers-plane geometry, sagittal plane wedging, and vertebral endplate concavity. A comparison of all four discs average height (mm), anterior–posterior (A–P) length (mm), lateral–lateral (L–L) length (mm), and ratio of A–P to L–L is shown in Table 1, and surface plots of heights of all four discs are shown in Figure 4.

3 | RESULTS

3.1 | Prediction of bovine caudal AF fiber angles

Optimizing the model to experimental measurements made at approximately mid-height across the full set of 16 discs yielded best-fit values of origin shift ($O = 0.8$ mm from the disc center toward posterior), fiber span angle at inner virtual lamella ($\theta_{SI} = 62.1°$), and span angle slope ($\Delta\theta_S = 70.7°$). Predicted fiber crossing angles (mean ± SD) at innermost, middle, and outermost virtual lamellae were 77.0 ± 5.8°, 55.6 ± 4.6° and 41.3 ± 1.7° respectively. Predicted net fiber angles at innermost, middle, and outermost virtual lamellae were −1.0 ± 5.4°, −0.9 ± 6.3° and −0.02 ± 1.6°, respectively. As shown in Figure 5, the relationship between all pairs of observed and predicted fiber crossing angles was fit by a 1:1 relationship with a coefficient of determination (R^2) of 0.967. This agreement was consistent across all areas of the disc.

The model was further used to predict variation of fiber angle with axial direction at a given circumferential and radial location. There was no clear pattern in the distribution of predicted net fiber angle in bovine caudal discs. Fiber crossing angle values were maximum at the innermost virtual lamella as compared to the outermost virtual lamella as shown in Figure 6. As expected, the nearly axisymmetric geometry of the bovine disc resulted in small variations in predicted fiber angle around the circumference of the AF along with minimal asymmetry between inclinations of right- and left-handed fibers.

3.2 | Prediction of human lumbar AF fiber angles

Fitting of the model to experimental fiber angle measurements in a human lumbar disc yielded optimal values of origin shift ($O = 4.8$ mm

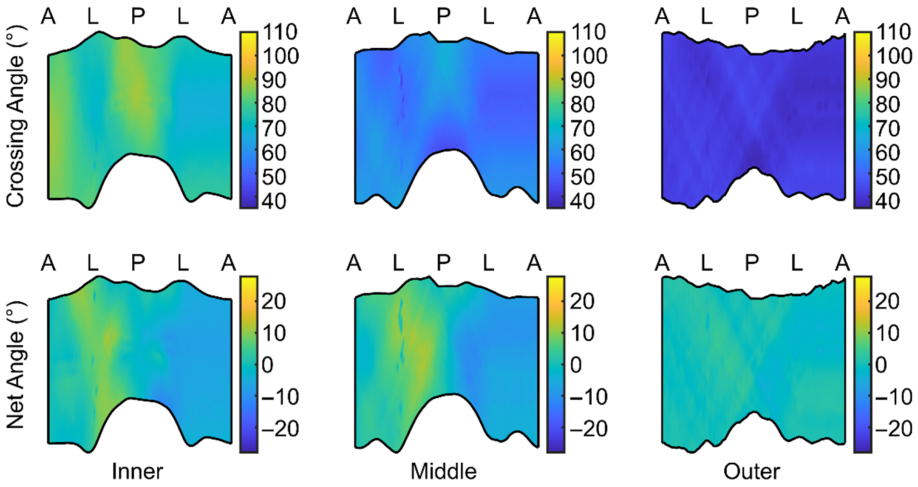

FIGURE 6 Contour plots of fiber crossing angle and net fiber angle in virtual lamellae of a representative bovine caudal disc. A, L, and P indicate anterior, lateral, and posterior, respectively.

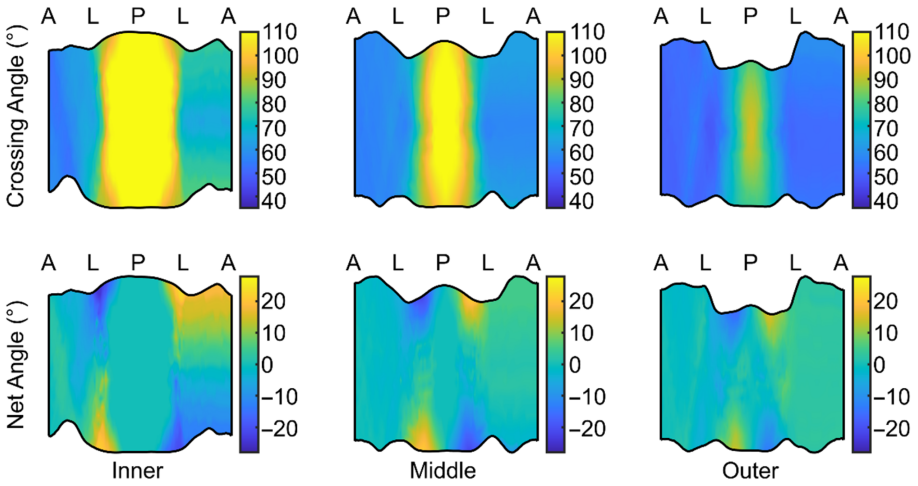

FIGURE 7 Contour plots of fiber crossing angle and net fiber angle in virtual lamellae of a representative L4L5 human IVD. A, L, and P indicate anterior, lateral, and posterior, respectively.

from the disc center toward posterior), fiber span angle at inner virtual lamella ($\theta_{SI} = 46.6°$), and span angle slope ($\Delta\theta_S = -1.7°$). Contour plots of crossing angle and net fiber angle and of human L4L5 lumbar IVD using these best-fit parameters at three virtual lamellae (innermost, middle, and outermost) are shown below (Figure 7).

Predicted fiber crossing angles (mean ± SD) at innermost lamella, middle lamella and outer most lamella were 86.3 ± 21.2°, 66.5 ± 11.5°, and 56.1 ± 5.4°, respectively. Predicted mean net fiber angles at innermost, middle. and outermost virtual lamella were 0.4 ± 6.6°, 0.3 ± 4.3°, and 0.4 ± 3°, respectively. The results (Figure 7) show that crossing angle values were maximum at the innermost virtual lamella as compared to the outermost and highest in the posterior region in all virtual lamellae. In general, crossing angle is predicted to vary more about the circumference in the inner AF than in the outer and more radially in the posterior than the anterior. Little variation in crossing angle with height is predicted. The predicted net angle values are maximum at the posterolateral region and are highest near the endplates. Net fiber angle is predicted to vary more near the endplates than near the mid-plane and more in the inner AF than in the outer. Note that while the range of net fiber angles in Figure 7 is from −20° to +20°, the similarly sized areas of positive and negative values result in a mean across each virtual lamella close to zero (~0.4°).

3.3 | Effect of disc geometry on prediction fiber angles

Spatial distributions of model predicted crossing angle and net fiber angle of human L1L2, L2L3, and L3L4 lumbar IVD geometries were similar to those shown in Figure 7 and are provided in the supplemental material, Data S1. Box plots of crossing angle and absolute value of net fiber angle of human four lumbar IVDs at three zones (inner, middle, outer virtual lamellae) are shown in Figures 8 and 9, respectively. While a substantial variation between levels was predicted, a clear trend from superior to inferior lumbar spine was not. At all levels, the median value of crossing angle was predicted to be highest at the inner zone, decreasing from inner to outer (Figure 8). Overall, in each zone, L4L5 had the highest predicted median crossing angle (Figure 9).

4 | DISCUSSION

The results confirm that the model can fit the radial trend in mid-plane fiber inclination in a set of bovine IVDs, for which endplate topographies are known, using a small number of subject-independent model parameters which represent the fiber distribution in an immature,

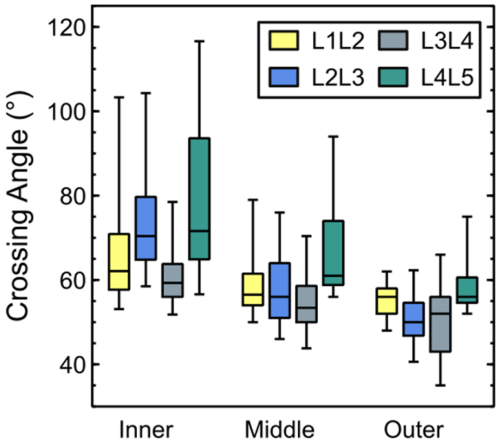

FIGURE 8 Box plots of fiber crossing angle values of L1L2, L2L3, L3L4, and L4L5 at three zones.

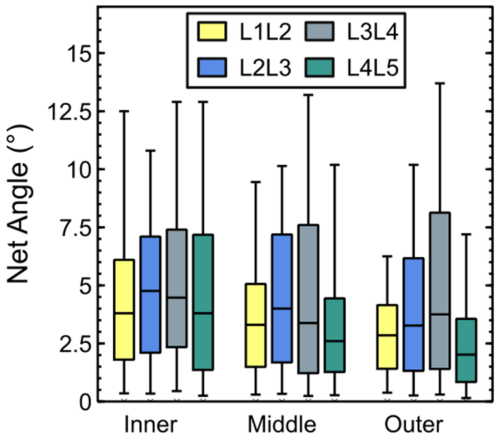

FIGURE 9 Box plots of net fiber angle values of L1L2, L2L3, L3L4, and L4L5 at three zones.

cylindrical state (θ_{SI} and $\Delta\theta_S$) and the location of the cylinder's axis relative to the axis of the mature spinal column (O). Furthermore, the model was able to recapitulate previously observed three-dimensional attributes of fiber orientations in the human AF, including areas of asymmetry between right- and left-handed orientations when similarly fit to mid-plane measurements. Additionally, prediction of AF fiber orientations in the human lumbar AF using a model predicated only on vertebral body growth supports our previous findings[10] suggesting that the orientations of fibers in the mouse caudal AF are not optimized to resist loading.

The present model generates a homogenous distribution of right- and left-handed fiber orientations. There are some additional attributes of the AF fiber arrangement that are not addressed directly. Most notably, the actual AF is separated into unidirectional lamellae, which vary in both thickness[7] and continuity.[12] Additionally, the model produces mean fiber orientations, about which there may be localized variability due to both fiber crimping[23] and derangement during disc degeneration.[24] These effects may be accounted for in future implementations of the model by adding stochastic terms to local fiber orientations. Other degenerative effects, such as height loss are incorporated into the model implicitly. While radial bulging was assumed to be minimal in this model, we have previously shown[10] that accounting for it changes best-fit parameter values, but not the distribution of mid-plane fiber orientations.

Prior application of the growth-based model to bovine tail discs in two dimensions found a best-fit value for angular span, θ_S, to be a constant 55.8°, which is considerably lower than the range of 62.1° (inner) to 132.8° (outer) in the present study. This is a direct result of the prior study using an estimated constant disc height value of 5 mm, while the present study used radiographically measured heights, which ranged from 5.8 to 8.5 mm. Additionally, the prior two-dimensional model suggested that the same constant angular span of 55.8° could be applied to human lumbar discs. However, best-ft values for a human lumbar disc using the three-dimensional model range from 46.6° (inner) to 44.9° (outer).

The present three-dimensional model predicts a much larger posterior shift in origin position (relative to disc center where disc center was halfway between the anterior and posterior) in the human lumbar disc than in bovine caudal. This is consistent with a requirement for more asymmetric growth in the human lumbar vertebra to account for the neural foramen. Similarly, the model predicts larger asymmetry between right- and left-handed fibers in human discs than in bovine, arising from the more complex shape of the human disc. In particular, prior work by Marchand and Ahmed[12] observed this asymmetry in the posterolateral aspect of the human lumbar disc, a phenomenon recapitulated by the model.

Applying the model to representative human lumbar discs, it is predicted that in all human disc levels, the fiber crossing angle decreases from the inner zone to the outer zone as previously observed,[7] and that the gradient from approximately 65° to 50° in the anterolateral and posterolateral AF reported by Cassidy et al., falls within our model predictions. While prior studies of fiber orientation in human discs did not test the effect of level, the variability in predicted mean fiber inclination angle between disc geometries in this study is comparable to that observed experimentally.[11]

The proposed model assumes a radial gradient of fiber angles separated into lamellae prior to vertebral body formation. Prior imaging of fibers in the developing disc have placed the separation into helical layers from the time of vertebral body condensation[25] to as late as locomotion.[26] Stabilization of length to diameter ratio in the growing notochord can, however, be used to infer helical patterning at earlier time points,[27] though this has not, to our knowledge, been directly observed. The exact biophysical cues which drive the formation of the lamellar structure of the AF remain an important and understudied topic. A possible mechanism of how this layered structure may arise is presented in Appendix. It should be noted that the model has thus far been compared to fairly sparse experimental data with nine locations each in 16 bovine discs and 18 locations in one human discs. Additionally, both experiments employed destructive techniques, which may have introduced

artifacts to the measurements. Further fitting to a more robust data set may be required for further model refinement.

Overall, the results of this study confirm the hypothesis that the three-dimensional fiber pattern of the intervertebral disc annulus fibrosus results from the growth of the spinal column. The proposed origin of the model input parameters at the early stages of growth suggest that they may be subject independent. If so, this spatial pattern may be accurately predicted by accounting for fiber deposition during early development (represented by angular span and angular span slope in the present model) along with the vertebral endplate topographies and origin offset resulting from growth into the mature spinal column.

ACKNOWLEDGMENTS

This work was funded by NSF Award# 2138342. The authors gratefully acknowledge Dr. Thomas Lufkin for manuscript comments.

CONFLICT OF INTEREST STATEMENT

The authors declare no conflicts of interest.

ORCID

Arthur J. Michalek https://orcid.org/0000-0001-9417-9344

REFERENCES

1. Elliott DM, Setton LA. Anisotropic and inhomogeneous tensile behavior of the human anulus fibrosus: experimental measurement and material model predictions. *J Biomech Eng*. 2001;123:256-263. doi:10.1115/1.1374202
2. Malandrino A, Noailly J, Lacroix D. Regional annulus fibre orientations used as a tool for the calibration of lumbar intervertebral disc finite element models. *Comput Methods Biomech Biomed Engin*. 2013;16:923-928. doi:10.1080/10255842.2011.644539
3. Momeni Shahraki N, Fatemi A, Goel VK, Agarwal A. On the use of biaxial properties in modeling annulus as a Holzapfel–Gasser–Ogden material. *Front Bioeng Biotechnol*. 2015;3:69. doi:10.3389/fbioe.2015.00069
4. Noailly J, Planell JA, Lacroix D. On the collagen criss-cross angles in the annuli fibrosi of lumbar spine finite element models. *Biomech Model Mechanobiol*. 2011;10:203-219. doi:10.1007/s10237-010-0227-5
5. Pickering E, Pivonka P, Little JP. Toward patient specific models of pediatric IVDs: a parametric study of IVD mechanical properties. *Front Bioeng Biotechnol*. 2021;9:1-12.
6. Ristaniemi A, Secerovic A, Grad S, Ferguson S. A novel fiber-reinforced poroviscoelastic bovine intervertebral disc finite element model for organ culture experiment simulations. *J Biomech Eng*. 2023;145:121006. doi:10.1115/1.4063557
7. Cassidy JJ, Hiltner A, Baer E. Hierarchical structure of the intervertebral disc. *Connect Tissue Res*. 1989;23:75-88. doi:10.3109/03008208909103905
8. Hickey DS, Hukins DW. Aging changes in the macromolecular organization of the intervertebral disc: an x-ray diffraction and electron microscopic study. *Spine*. 1982;7:234-242. doi:10.1097/00007632-198205000-00007
9. Michalek AJ. A growth-based model for the prediction of fiber angle distribution in the intervertebral disc annulus fibrosus. *Biomech Model Mechanobiol*. 2019;18:1363-1369. doi:10.1007/s10237-019-01150-4
10. Raza A, Michalek AJ. Radial trend in murine annulus fibrosus fiber orientation is best explained by vertebral growth. *Eur Spine J*. 2021;30:3450-3456. doi:10.1007/s00586-021-06999-7
11. Stein D, Assaf Y, Dar G, et al. 3D virtual reconstruction and quantitative assessment of the human intervertebral disc's annulus fibrosus: a DTI tractography study. *Sci Rep*. 2021;11:6815. doi:10.1038/s41598-021-86334-8
12. Marchand F, Ahmed AM. Investigation of the laminate structure of lumbar disc anulus fibrosus. *Spine*. 1990;15:402-410. doi:10.1097/00007632-199005000-00011
13. Heuer F, Schmidt H, Wilke H-J. The relation between intervertebral disc bulging and annular fiber associated strains for simple and complex loading. *J Biomech*. 2008;41:1086-1094. doi:10.1016/j.jbiomech.2007.11.019
14. Ebeling U, Reulen HJ. Are there typical localisations of lumbar disc herniations? A prospective study. *Acta Neurochir (Wien)*. 1992;117:143-148. doi:10.1007/BF01400611
15. Holzapfel GA, Schulze-Bauer CAJ, Feigl G, Regitnig P. Single lamellar mechanics of the human lumbar anulus fibrosus. *Biomech Model Mechanobiol*. 2005;3:125-140. doi:10.1007/s10237-004-0053-8
16. Disney CM, Eckersley A, McConnell JC, et al. Synchrotron tomography of intervertebral disc deformation quantified by digital volume correlation reveals microstructural influence on strain patterns. *Acta Biomater*. 2019;92:290-304. doi:10.1016/j.actbio.2019.05.021
17. Stadelmann MA, Maquer G, Voumard B, et al. Integrating MRI-based geometry, composition and fiber architecture in a finite element model of the human intervertebral disc. *J Mech Behav Biomed Mater*. 2018;85:37-42. doi:10.1016/j.jmbbm.2018.05.005
18. Berg-Johansen B, Fields AJ, Liebenberg EC, Li A, Lotz JC. Structure–function relationships at the human spinal disc-vertebra interface. *J Orthop Res*. 2018;36:192-201. doi:10.1002/jor.23627
19. Brown S, Rodrigues S, Sharp C, et al. Staying connected: structural integration at the intervertebral disc-vertebra interface of human lumbar spines. *Eur Spine J*. 2017;26:248-258. doi:10.1007/s00586-016-4560-y
20. François RJ, Dhem A. Microradiographic study of the normal human vertebral body. *Acta Anat (Basel)*. 1974;89:251-265. doi:10.1159/000144288
21. Rodrigues SA, Thambyah A, Broom ND. How maturity influences annulus-endplate integration in the ovine intervertebral disc: a micro- and ultra-structural study. *J Anat*. 2017;230:152-164. doi:10.1111/joa.12536
22. Duclos SE, Denning SK, Towler C, Michalek AJ. Level-wise differences in in vivo lateral bending moment are associated with microstructural alterations in bovine caudal intervertebral discs. *J Exp Biol*. 2020;223:1-10. doi:10.1242/jeb.229971
23. Vergari C, Chan D, Clarke A, Mansfield JC, Meakin JR, Winlove PC. Bovine and degenerated human annulus fibrosus: a microstructural and micromechanical comparison. *Biomech Model Mechanobiol*. 2017;16:1475-1484. doi:10.1007/s10237-017-0900-z
24. Gruber HE, Hanley EN. Observations on morphologic changes in the aging and degenerating human disc: secondary collagen alterations. *BMC Musculoskelet Disord*. 2002;3:9. doi:10.1186/1471-2474-3-9
25. Ghazanfari S, Werner A, Ghazanfari S, Weaver JC, Smit TH. Morphogenesis of aligned collagen fibers in the annulus fibrosus: mammals versus avians. *Biochem Biophys Res Commun*. 2018;503:1168-1173. doi:10.1016/j.bbrc.2018.06.136
26. Grotmol S, Kryvi H, Keynes R, Krossøy C, Nordvik K, Totland GK. Stepwise enforcement of the notochord and its intersection with the myoseptum: an evolutionary path leading to development of the

vertebra? *J Anat*. 2006;209:339-357. doi:10.1111/j.1469-7580.2006.00618.x

27. Adams DS, Keller R, Koehl MAR. The mechanics of notochord elongation, straightening and stiffening in the embryo of *Xenopus laevis*. *Development*. 1990;110:115-130. doi:10.1242/dev.110.1.115
28. Boyd JD. Biophysical control of microfibril orientation in plant cell walls. *Forestry Sciences*. Springer Netherlands; 1985. doi:10.1007/978-94-009-5065-8
29. Wang Q, Huang H, Wei K, Zhao Y. Time-dependent combinatory effects of active mechanical loading and passive topographical cues on cell orientation. *Biotechnol Bioeng*. 2016;113:2191-2201. doi:10.1002/bit.25981

SUPPORTING INFORMATION

Additional supporting information can be found online in the Supporting Information section at the end of this article.

How to cite this article: Raza A, Howell GT, Michalek AJ. Three-dimensional fiber patterning in the annulus fibrosus can be derived from vertebral endplate topography. *JOR Spine*. 2024;7(3):e1361. doi:10.1002/jsp2.1361

APPENDIX: A PROPOSED MECHANISM FOR LAYERED HELICAL PATTERNING IN THE DEVELOPING AF

The following proposes a qualitative model describing a potential process through which cell proliferation on the surface of a cylinder subjected to internal pressurization will result in a lamellar structure. It is conceptually similar to the model previously proposed by Boyd to describe layered cellulose fiber deposition in plant cell walls[28] and presumes that cell proliferation on the surface of the developing notochordal sheath is guided by strains resulting from hydraulic swelling of the notochord.

As schematically represented in Figure A1, the magnitude and the polar distribution of axial strains in a biaxially loaded tissue are dictated by both the magnitudes of applied stresses (σ_1, σ_2) and material anisotropy driven by aligned fibers. For a given state of plane stress, peak strain in an isotropic material will correspond to the direction of the first principal stress (σ_1). Addition of a low density of aligned fibers will stiffen the tissue in the fiber direction, resulting in an increase in peak strain with a shift in direction toward that perpendicular to the fiber orientation. A high density of aligned fibers will increase material anisotropy, bringing peak strain orientation closer to perpendicular to fiber orientation. It is assumed here that AF progenitor cells behave as fibroblasts and may be aligned by either linear surface patterning or by axial strain. Below a threshold axial strain cells proliferating on the surface of the cylinder will align with orientation of surface fibers, and above it they will align with the direction of peak strain.[29] These simple assumptions, applied to the osmotic swelling of a cylinder, are sufficient to produce the AF structure through the process described below and shown in Figure A2.

Upon initial closure of the notochordal sheath (Figure A2A), cells will form rings and begin depositing extracellular matrix fibers in a shallowly pitched winding around the circumference,[25] resulting in an anisotropic material with a higher elastic modulus in the circumferential direction than in the axial. Osmotic pressurization of the notochord will thus result in axial elongation (Figure A2B), which will pull the circumferential fibers into a helical arrangement.[28] Deposition of subsequent fibers will follow those of the existing substrate, however, increasing material anisotropy will cause osmotic pressure to deform the cylinder into a corkscrew shape (Figure A2C) with handedness opposite to that of the dominant fiber orientation. In the illustrated example, the single population of left-handed fibers in (Figure A2B) will result in a right-handed corkscrew in (Figure A2C). When strain reaches a threshold value (Figure A2D), cells proliferating on the surface begin to align with the direction of maximum strain, depositing a new layer of fibers in a helical pattern with handedness opposite to that of the layer below. In this case, that layer will be right-handed.

Deposition of fibers in this layer will reduce material anisotropy, straightening the cylinder (Figure A2E,F). However, as fiber deposition continues the material will become anisotropic again, causing the cylinder to return to a corkscrew shape (Figure A2G), now of handedness

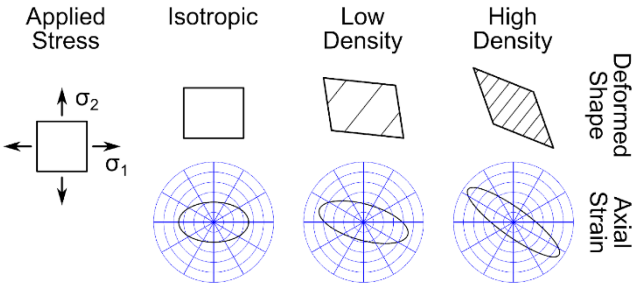

FIGURE A1 Both magnitudes of applied principal stresses and tissue anisotropy arising from density of aligned fibers dictate polar distributions of axial strain.

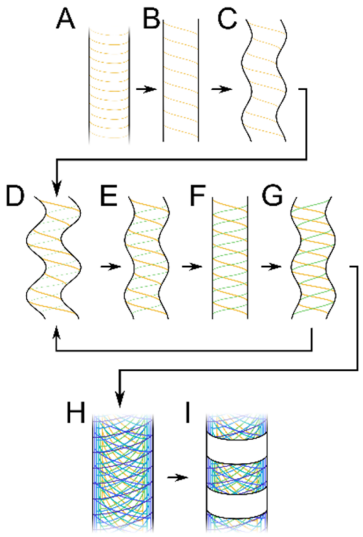

FIGURE A2 Theoretical basis for the development of lamellar pattern (A–H) followed by segmentation (I).

opposite to that of fibers in the second layer. As this cycle repeats, the notochordal sheath will develop concentric layers with opposite fiber handedness (Figure A2H). It should be noted that the point of maximum distortion from cylindrical (Figure A2D), splitting of the surface sheet may occur resulting in incomplete layers.[12] Continued elongation of the cylinder during this cycle will result in a decrease in helical pitch from the inner to the outer wall.[28] While this process is schematically represented as a semi-infinite cylinder in Figure A2, layers may continue to accumulate after vertebral body condensations begin to form.[25] This may impose additional constraints on surface strains. Within established layers, cell proliferation and fiber deposition will continue to favor the existing fiber orientation. Though this process has not yet been corroborated experimentally, it is sufficient to produce the immature state fiber angle distributions used in the preceding model. Furthermore, the prior observation of more rapid growth in diameter in the central portion of the notochord than toward the ends,[25] then explains the discrepancy between best-fit lumbar and caudal span angles in the model.